

# Integrated Intercalation-Based and Interfacial Sodium Storage in Graphene-Wrapped Porous $\text{Li}_4\text{Ti}_5\text{O}_{12}$ Nanofibers Composite Aerogel

Chaoji Chen, Henghui Xu, Tengfei Zhou, Zaiping Guo, Lineng Chen, Mengyu Yan, Liqiang Mai, Pei Hu, Shijie Cheng, Yunhui Huang,\* and Jia Xie\*

Sodium storage in both solid–liquid and solid–solid interfaces is expected to extend the horizon of sodium-ion batteries, leading to a new strategy for developing high-performance energy-storage materials. Here, a novel composite aerogel with porous  $\text{Li}_4\text{Ti}_5\text{O}_{12}$  (PLTO) nanofibers confined in a highly conductive 3D-interconnected graphene framework (G-PLTO) is designed and fabricated for Na storage. A high capacity of  $195 \text{ mA h g}^{-1}$  at  $0.2 \text{ C}$  and super-long cycle life up to 12 000 cycles are attained. Electrochemical analysis shows that the intercalation-based and interfacial Na storage behaviors take effect simultaneously in the G-PLTO composite aerogel. An integrated Na storage mechanism is proposed. This study ascribes the excellent performance to the unique structure, which not only offers short pathways for  $\text{Na}^+$  diffusion and conductive networks for electron transport, but also guarantees plenty of PLTO–electrolyte and PLTO–graphene interfacial sites for  $\text{Na}^+$  adsorption.

## 1. Introduction

Over the last decade, rechargeable lithium-ion batteries (LIBs) have been attracting intense interests as ever-increasing concerns in renewable energy storage for intermittent energy sources such as solar and wind energy.<sup>[1]</sup> However, the fast growing demands for LIBs have led to the upsurge in the price of the lithium precursors. In addition, the limit resource of lithium is also an obstacle for the extension of LIBs to massive energy storage. Recently, tremendous efforts have been devoted to developing rechargeable batteries beyond LIBs to meet the demands of large-scale energy storage.<sup>[4]</sup> Among them, rechargeable sodium-ion battery (SIB) represents one of the most

promising alternatives due to low cost, abundant resource of sodium on earth and the property similarity between sodium and lithium. Recent investigations on SIB cathodes have mainly concentrated on materials such as Prussian blue,<sup>[10,11]</sup>  $\text{Na}_x\text{CoO}_2$ ,<sup>[12]</sup>  $\text{Na}_3\text{V}_2(\text{PO}_4)_3$ ,<sup>[13]</sup> and  $\text{Na}_2\text{FePO}_4\text{F}$ .<sup>[14]</sup> In the case of anodes,<sup>[15]</sup> carbonaceous materials are the most intensively investigated ones.<sup>[16–21]</sup> Despite the insufficient kinetics for  $\text{Na}^+$  intercalating into the unmodified graphite carbon due to its thermodynamically unfavorable structure toward  $\text{Na}^+$  insertion,<sup>[8]</sup> hard carbons with more disorder structure possessing viable capacity and cycling performance represent the promising prospect.<sup>[17–21]</sup> However, the operating voltage in hard carbons is too low (near zero versus  $\text{Na}^+/\text{Na}$ ), which may rise safety concerns by Na metal dendrite formation, especially at high current rates. Based on this consideration, Ti-based compounds with a relatively higher operating voltage have been regarded as alternative candidates, for instance,  $\text{TiO}_2$  (including both anatase and bronze phases),<sup>[22]</sup>  $\text{Na}_2\text{Ti}_3\text{O}_7$ ,<sup>[25]</sup>  $\text{NaTiO}_2$ ,<sup>[26]</sup> and  $\text{K}_{0.8}\text{Ti}_{1.73}\text{Li}_{0.27}\text{O}_4$ .<sup>[27]</sup> The issues these candidates facing are the relatively low capacity and unsatisfied rate capability because of limited  $\text{Na}^+$  storage capability in the host structure and the low instinct conductivity for both  $\text{Na}^+$  ions and electrons.

Recently, Sun et al.<sup>[28]</sup> reported the  $\text{Na}^+$  insertion into spinel  $\text{Li}_4\text{Ti}_5\text{O}_{12}$  (LTO) with an average operating voltage of  $\approx 0.9 \text{ V}$  and reversible capacity of  $\approx 155 \text{ mA h g}^{-1}$  at  $0.1 \text{ C}$ . A mechanism of three-phase separation is disclosed as  $2 \text{ Li}_4\text{Ti}_5\text{O}_{12} + 6 \text{ Na} + 6 \text{ e} \leftrightarrow \text{Li}_7\text{Ti}_5\text{O}_{12} + \text{Na}_6\text{LiTi}_5\text{O}_{12}$ , with a theoretical

Dr. C. Chen, Dr. P. Hu, Prof. S. Cheng, Prof. J. Xie  
State Key Laboratory of Advanced  
Electromagnetic Engineering and Technology  
School of Electrical and Electronic Engineering  
Huazhong University of Science and Technology  
Wuhan 430074, P. R. China  
E-mail: xiejia@hust.edu.cn

Dr. H. Xu, Prof. Y. Huang  
State Key Laboratory of Materials Processing  
and Die and Mould Technology  
School of Materials Science and Engineering  
Huazhong University of Science and Technology  
Wuhan 430074, P. R. China  
E-mail: huangyh@hust.edu.cn

T. Zhou, Prof. Z. Guo  
Institute for Superconducting and Electronic Materials  
Australian Institute for Innovative Materials (AIIM)  
School of Mechanical, Materials and Mechatronics Engineering  
University of Wollongong  
North Wollongong, NSW, Australia

L. Chen, M. Yan, Prof. L. Mai  
State Key Laboratory of Advanced Technology for  
Materials Synthesis and Processing  
WUT-Harvard Joint Nano Key Laboratory  
Wuhan University of Technology  
Wuhan 430070, P. R. China

Prof. Y. Huang, Prof. J. Xie  
Collaborative Innovation Center of Intelligent New Energy Vehicle  
Tongji University  
Shanghai 201804, P. R. China



DOI: 10.1002/aenm.201600322

capacity of  $175 \text{ mA h g}^{-1}$ . In this context, LTO is potentially available as a safe and high-performance anode for SIBs. For practical applications, significant challenges still remain by considering the intrinsically low ionic and electronic conductivity of LTO. Additionally, as the ionic radius of  $\text{Na}^+$  is larger than that of  $\text{Li}^+$ , one can imagine that it would be harder for  $\text{Na}^+$  inserting into LTO than  $\text{Li}^+$ .

Recent works have demonstrated that interfacial Li or Na storage may occur when viable solid–liquid or solid–solid interfaces are designed in the battery system by constructing either porous structure or mixed phase composition.<sup>[29]</sup> Such interfacial Li or Na storage not only contributes to an excess capacity of the electrode, but also characterizes a capacitive feature that is favorable to achieving a high rate capability and long cycling life. In this regard, rational structure designs involving pore structure and phase composition represent an effective direction toward high-performance batteries.

Herein we report a novel composite aerogel with integrated design of pore structure and mixed phase composition, in which porous LTO (PLTO) nanofibers are confined in the highly conductive 3D interconnected graphene frameworks (G-PLTO). Such integrated structure design offers not only short pathways for  $\text{Na}^+$  diffusion and conductive networks for electron transport but also plenty of interfacial sites for interfacial Na storage. The combination of intercalation-based and interfacial Na storage contributes to a high reversible capacity of  $195 \text{ mA h g}^{-1}$  at 0.2 C, exceeding the theoretical capacity of LTO. Furthermore, the unique structure is highly stable upon long-term cycling and

beneficial for the formation of a stable solid electrolyte interphase (SEI) layer, which conduce to an ultralong cycle life of 12 000 cycles for the G-PLTO electrode. These findings provide new insights into high-performance sodium-ion batteries for large-scale energy storage applications.

## 2. Results and Discussion

PLTO nanofibers constructed by numerous nanoparticles were synthesized via an electrospinning method followed by a post-annealing process, as described in detail in our previous work.<sup>[34]</sup> The subsequent hybridization of PLTO with graphene oxide (GO) to form a 3D G-PLTO composite aerogel was achieved by dispersing PLTO into GO solution, heat-treating via a hydrothermal route with addition of ethylenediamine (EDA), and finally freeze-drying. **Figure 1a** graphically illustrates the fabrication process of G-PLTO and its structural profile for Na storage. Because of the electrostatic attraction between the negative-charge GO and positive-charge PLTO nanofibers, an evenly dispersed suspension is formed (**Figure 1b**). Under the hydrothermal treatment, EDA could reduce GO into graphene and at the same time crosslink the graphene sheets with volumetric shrinkage, giving rise to the formation of G-PLTO hydrogel (**Figure 1c**). After freeze-drying, the 3D interconnected structure can be well maintained (**Figure 1d**). **Figure 1e** shows the fibrous morphology of the electrospun LTO fibers. With a higher magnification, it can be clearly observed

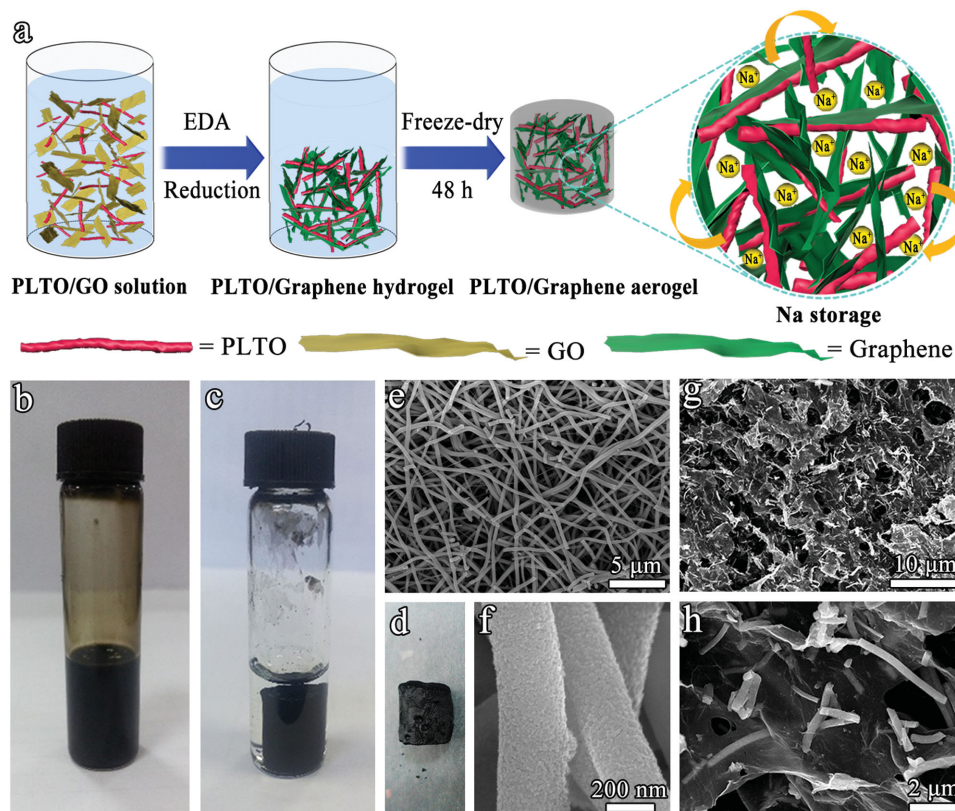


**Figure 1.** a) Graphic illustration of the formation process of the G-PLTO aerogel. b–d) Photographs of the PLTO/GO suspension, PLTO/G hydrogel and aerogel, respectively. e,f) SEM images of the PLTO product. g,h) SEM images of the G-PLTO composite aerogel.

that each individual LTO fiber is constructed by numerous nanoparticles and nanopores, thus possessing a porous structure (Figure 1f and Figure S1, Supporting Information).<sup>[34]</sup> The morphology of the G-PLTO aerogel is revealed by scanning electron microscopy (SEM, Figure 1g), showing that graphene sheets connect with each other to form a 3D interconnected porous structure, where numerous LTO nanofibers are confined. A higher-magnified SEM image shows that LTO nanofibers are wrapped by the graphene sheet (Figure 1h).

More details of the structure for the G-PLTO composite aerogel can be provided by transmission electron microscopy (TEM) in Figure 2. On the surface of the LTO fiber, a thin layer of graphene can be clearly observed (Figure 2a–c). Meanwhile, the nanoparticles-constructed porous structure of the LTO fiber can be further evidenced (Figure 2b). High-resolution TEM (HR-TEM) image in Figure 2c shows clear lattices with a spacing of 0.48 nm, which can be assigned to the (111) plane of spinel  $\text{Li}_4\text{Ti}_5\text{O}_{12}$ . The spinel  $\text{Li}_4\text{Ti}_5\text{O}_{12}$  phase structure can be further identified by the powder X-ray diffraction (XRD, Figure S2, Supporting Information) and Raman spectroscopy (Figure S3, Supporting Information) measurements. We should also note that Raman spectrum of the G-PLTO composite aerogel shows strong D and G peaks in addition to characteristic peaks of the  $\text{Li}_4\text{Ti}_5\text{O}_{12}$  phase, confirming the existence of graphene in the composite aerogel. The scanning transmission electron microscopy (STEM) image and the corresponding Ti, O, C element mapping images reveal the homogenous distribution of Ti and O elements in the fiber and C element in the surface wrapped graphene (Figure 2d,e). The carbon content in the composite aerogel is quantified to be  $\approx 20$  wt% based on the thermogravimetry (TG) analysis (Figure S4, Supporting Information).

The electrochemical sodium storage behaviors and performances of the G-PLTO composite aerogel and pure PLTO were evaluated in Na-half cell. The cyclic voltammetry (CV) curves for the initial 3 cycles at  $0.1 \text{ mV s}^{-1}$  of PLTO and G-PLTO are shown in Figure 3a,b, respectively. In both cases, a peak below 0.5 V can be observed in the first cycle and disappears in the subsequent cycling process. This may be related to the formation of a SEI layer on the electrode surface in the initial cycle.<sup>[4,35]</sup> A pair of reduction/oxidation peaks at 0.63/1.06 V for PLTO and 0.75/1.0 for G-PLTO can be seen in the first and subsequent cycles, which are assigned to the  $\text{Na}^+$  insertion/extraction into/out of the  $\text{Li}_4\text{Ti}_5\text{O}_{12}$  host structure ( $\text{Li}_4\text{Ti}_5\text{O}_{12} \leftrightarrow \text{Na}_6\text{LiTi}_5\text{O}_{12}$ ).<sup>[28,36,37]</sup> It is interesting to note that the peak separation value ( $\Delta E$ ) for G-PLTO is much smaller than that of PLTO (0.25 V vs 0.43 V), indicating that the overpotential or energy necessary for  $\text{Na}^+$  insertion into PLTO is much higher than that of G-PLTO.

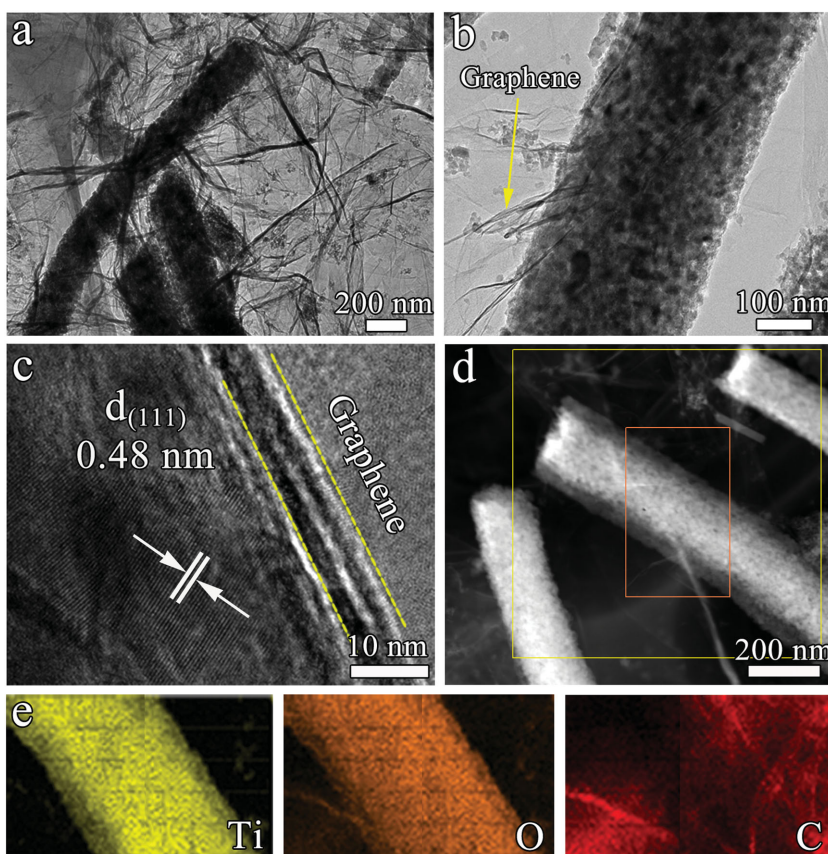


**Figure 2.** a,b) TEM, c) HR-TEM, d) STEM images and the corresponding Ti, O, e) C element mapping images for the G-PLTO composite aerogel.

This demonstrates that hybridizing PLTO with the highly conductive 3D interconnected graphene frameworks can efficiently reduce the resistance of transporting  $\text{Na}^+$  ions and electrons. The representative galvanostatic cycling profiles of the PLTO (Figure 3c) and G-PLTO (Figure 3d) electrodes obtained at 0.2 C exhibit similar features on discharge with a sloping region (I) from open circuit voltage (OCV) down to  $\approx 0.75$  V, a plateau (II) at  $\approx 0.75$  V and another sloping region (III) from  $\approx 0.75$  down to 0.05 V. Regions I and II are related to the  $\text{Na}^+$  insertion into the  $\text{Li}_4\text{Ti}_5\text{O}_{12}$  host structure whereas Region III to the interfacial Na storage occurring in the solid–liquid and solid–solid interfaces of the battery system. By comparing the capacity contributions from the three regions (Figure 3e,f), we can conclude that the  $\text{Na}^+$  ions stored through both insertion and interfacial adsorption in G-PLTO are much more than those in PLTO, giving rise to a much higher capacity for G-PLTO ( $195 \text{ mA h g}^{-1}$ ) than that for PLTO ( $110 \text{ mA h g}^{-1}$ ). Interestingly, the value of  $195 \text{ mA h g}^{-1}$  exceeds the theoretical capacity of  $\text{Li}_4\text{Ti}_5\text{O}_{12}$  ( $175 \text{ mA h g}^{-1}$ ), which should be attributed to the additional interfacial Na storage occurring in the interfaces of  $\text{Li}_4\text{Ti}_5\text{O}_{12}$ –electrolyte, graphene–electrolyte and  $\text{Li}_4\text{Ti}_5\text{O}_{12}$ –graphene. This will be discussed later in more details. It is not surprising that the gap between the discharged and charged plateaus for G-PLTO (0.25 V) is much smaller than that of PLTO (0.4 V), agreeing well with the CV observations.

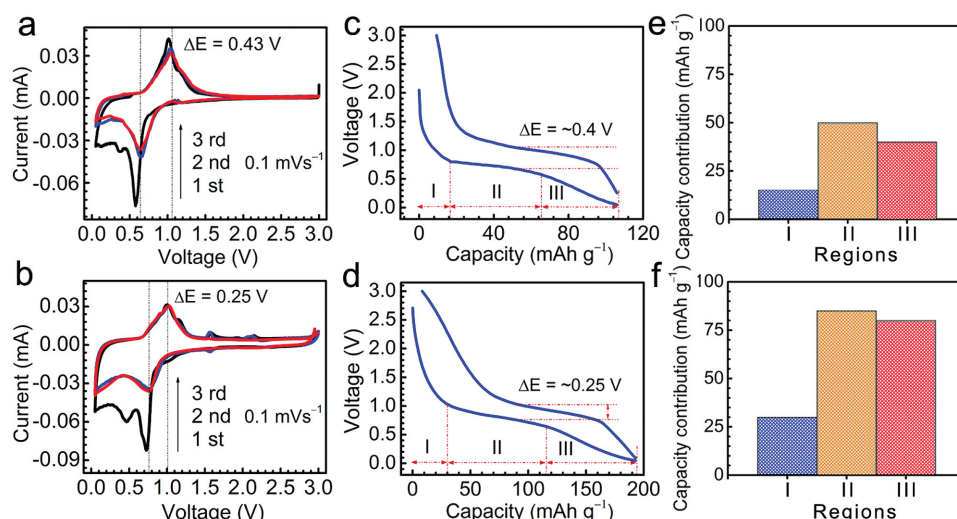


**Figure 3.** a,b) CV curves of the initial three cycles at  $0.1 \text{ mV s}^{-1}$ , c,d) charge–discharge profiles at  $0.2 \text{ C}$ , and e,f) capacity contributions from Regions I to III for the PLTO (up) and G-PLTO (down) electrodes.

**Figure 4** shows the sodium storage performance of the G-PLTO electrode. The G-PLTO electrode exhibits reversible capacities of  $200, 180, 145, 115, 80,$  and  $58 \text{ mA h g}^{-1}$  at  $0.2, 0.6, 1.2, 3, 6,$  and  $12 \text{ C}$ , respectively, indicating an excellent rate capability. Even at the extremely high rate of  $60 \text{ C}$ , a reversible capacity is still retained at  $35 \text{ mA h g}^{-1}$ . When the current rate is reset back to  $0.2 \text{ C}$  after cycling at various rates, the capacity can be recovered up to  $195 \text{ mA h g}^{-1}$ , and keeps almost steady in the subsequent  $115$  charge–discharge cycles (Figure 4b), demonstrating good cyclability. The charge–discharge profiles at different C-rates show similar shapes consisting of two sloping regions and one plateau region, indicative of stable host structure even over fast  $\text{Na}^+$  insertion/extraction (Figure 4c). Besides, as the current rate increases, the voltage plateaus decrease apparently, but the sloping region keeps almost unchanged. These results suggest that the kinetics of  $\text{Na}^+$  intercalation into  $\text{Li}_4\text{Ti}_5\text{O}_{12}$  becomes insufficient at high

rates while the kinetics of  $\text{Na}^+$  adsorption on the interface (interfacial Na storage) remain highly sufficient even at high rates. The G-PLTO electrode also demonstrates superior durability. After slow decay in the initial 10 cycles, the reversible capacity of  $120 \text{ mA h g}^{-1}$  keeps steady even after  $12\,000$  cycles at  $3 \text{ C}$  (Figure 4d). As far as we know, this is the longest reported cycle life up to date for the Ti-based electrodes of SIBs, and one of the best cyclabilities among all ever-reported electrodes of SIBs (see Table S1 in the Supporting Information).<sup>[4,10–28,36–38]</sup> We should also note that the initial Coulombic efficiency is not very high ( $\approx 41\%$ ), which may be due to the SEI formation on the surface of the electrode material in the first cycle.<sup>[4,35]</sup> Strategies such as pre-sodiation, chemical treating or adding additives (such as fluorinated ethylene carbonate (EC)) to the electrolyte have been reported to efficiently mitigate the irreversible capacity.<sup>[4,23,39]</sup> For comparison, we have also investigated the Na storage performances of the PLTO and the graphene

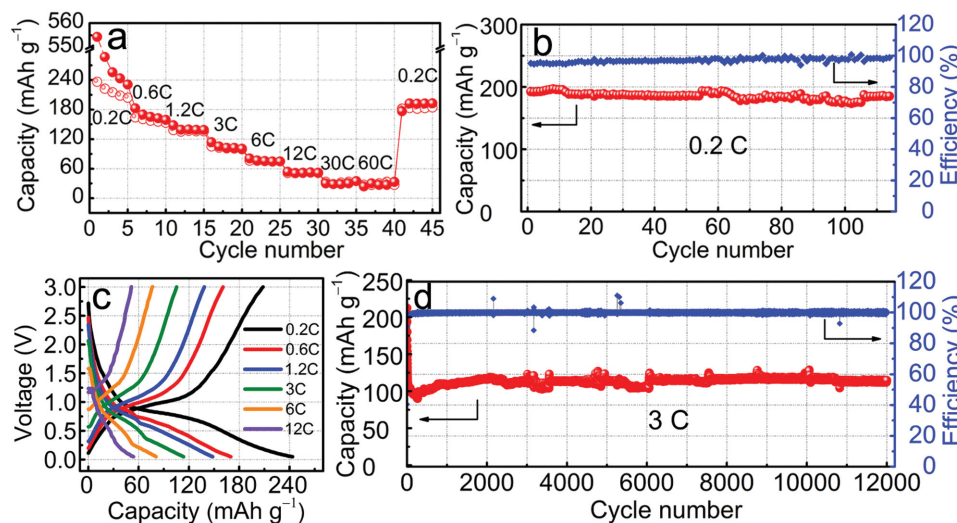


**Figure 4.** Sodium storage performance of the G-PLTO electrode: a) rate performance at various C-rates, b) cycling performance at  $0.2 \text{ C}$  after the rate performance test in (a), c) discharge profiles from various C-rates of  $0.2$ – $12 \text{ C}$ , and d) long-term cycling performance at  $3 \text{ C}$  for  $12\,000$  cycles.

aerogel (GA, fabricated in the same procedure as G-PLTO except no PLTO added) electrodes. The PLTO electrode shows a much poorer rate performance with capacities of 100, 75, 50, 30, 20, 15, 12, and 10 mA h g<sup>-1</sup> at 0.2, 0.6, 1.2, 3, 6, 12, 30, and 60 C (Figure S5a, Supporting Information). For the PLTO electrode, the capacity is only 90 mA h g<sup>-1</sup> at 0.2 C (Figure S5b, Supporting Information), and the performance gets worse at a higher rate of 3 C (the capacity decreases from 80 to 35 mA h g<sup>-1</sup> after 500 cycles, see Figure S5c in the Supporting Information). The inferior performance of PLTO may result from its low intrinsic conductivity toward Na<sup>+</sup> ions and electrons. The rate performance of the GA electrode is unsatisfied as well, demonstrated by capacities of 150, 120, 110, 90, 75, 58, 35, and 25 mA h g<sup>-1</sup> at 0.2, 0.6, 1.2, 3, 6, 12, 30, and 60 C (1 C = 175 mA g<sup>-1</sup>), respectively (Figure S6a, Supporting Information). A low capacity of ≈80 mA h g<sup>-1</sup> is obtained at 3 C over 200 cycles (Figure S6b, Supporting Information). Considering the fact that the mass percentage of the graphene framework in the G-PLTO composite is only 20 wt%, the capacity contribution from the graphene framework would be very small (see Table S2 in the Supporting Information).

The big difference in sodium storage performance between the G-PLTO composite aerogel and the pure PLTO or GA materials further proves the effect caused by confining porous Li<sub>4</sub>Ti<sub>5</sub>O<sub>12</sub> nanofibers in the highly conductive 3D interconnected graphene frameworks. From a structural point of view, the composite structure shows three advantages. Firstly, the porous architecture of LTO nanofibers consisting of numerous nanoparticles and nanopores not only contributes to sufficient contact between LTO and electrolyte but also shortens the pathway for Na<sup>+</sup> diffusion, which is beneficial to the Na<sup>+</sup> insertion/extraction process and the interfacial Na storage on the LTO–electrolyte interface. Secondly, the strong adhesion between LTO nanofibers and graphene frameworks offers abundant interfacial sites for Na<sup>+</sup> adsorption, contributing to additional interfacial Na storage. Thirdly, the 3D interconnected graphene frameworks provide highly conductive networks for fast transport of electrons, lowering the resistance for Na storage, which can also be confirmed by the EIS results of the G-PLTO and PLTO electrodes (Figure S7, Supporting Information). **Figure 5** graphically illustrates the structural merits for Na storage in the G-PLTO composite aerogel. It clearly demonstrates that the integrated structure design involving hierarchical pores (nanopores among the LTO nanoparticles and macropores among the graphene sheets) and mixed phase composition (LTO and graphene phases) conduces to a combinational Na storage mechanism for Na<sup>+</sup> insertion/extraction and interfacial Na storage.

Therefore, the superior Na storage performance of the G-PLTO composite aerogel is greatly ascribed to the interfacial Na storage occurring in the plenty PLTO–electrolyte and PLTO–graphene interfaces. To validate this, we performed kinetic

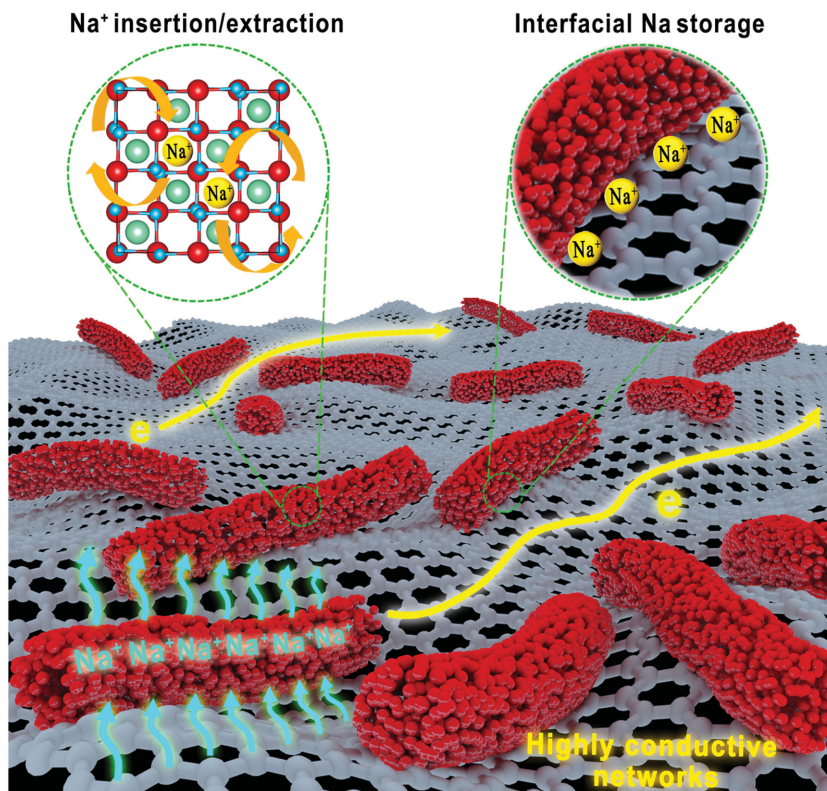


**Figure 5.** Graphical illustration of the structural merits and the integrated Na storage mechanisms in the G-PLTO electrode.

analysis based on cyclic voltammetry that has been proven as a powerful technique for studying the electrochemical kinetics of electrode materials toward Li<sup>+</sup> or Na<sup>+</sup>. **Figure 6a,c** display the typical CV curves at the scan rates of 0.1–2 and 5–100 mV s<sup>-1</sup>, respectively, where broad peaks during both cathodic and anodic processes can be observed. It is interesting to note that the redox peak separation value keep almost identical (≈0.25 V) when the scan rate is lower than 2 mV s<sup>-1</sup>, demonstrating small polarization at moderate scan rates. When the scan rate goes above 2 mV s<sup>-1</sup> (from 5 to 100 mV s<sup>-1</sup>), the peak separation value increases with the scan rate, indicating a higher energy needed for Na<sup>+</sup> intercalation at a higher rate. According to the relationship of  $i = av^b$  between current ( $i$ ) and scan rate ( $v$ ), it is possible to determine the  $b$ -value by plotting the  $\log(i)$ – $\log(v)$  curve.<sup>[4,40,41]</sup> If the  $b$ -value is 1, the total charge ( $Q$ ) comes from the capacitive process (interfacial Na storage process); if  $b = 0.5$ , the charge is totally diffusion-controlled (Na<sup>+</sup> insertion/extraction process). As shown in Figure 6b, the  $b$ -value is 0.87 both in the cathodic and anodic processes when  $v < 2$  mV s<sup>-1</sup>, indicating that the charge (thus the capacity) comes from two types of contributions. When the scan rate is higher than 2 mV s<sup>-1</sup>, the  $b$ -value significantly decreases from 0.84 to 0.52 (Figure 6d), reflecting the limitation to the rate capability which may be resulted from the increase of the ohmic contribution and/or diffusion constrains at high rates.<sup>[41]</sup> With a more detailed analysis, we can further quantify the exact ratio between the two contributions at a certain scan rate by separating the specific contribution from the capacitive and diffusion-controlled

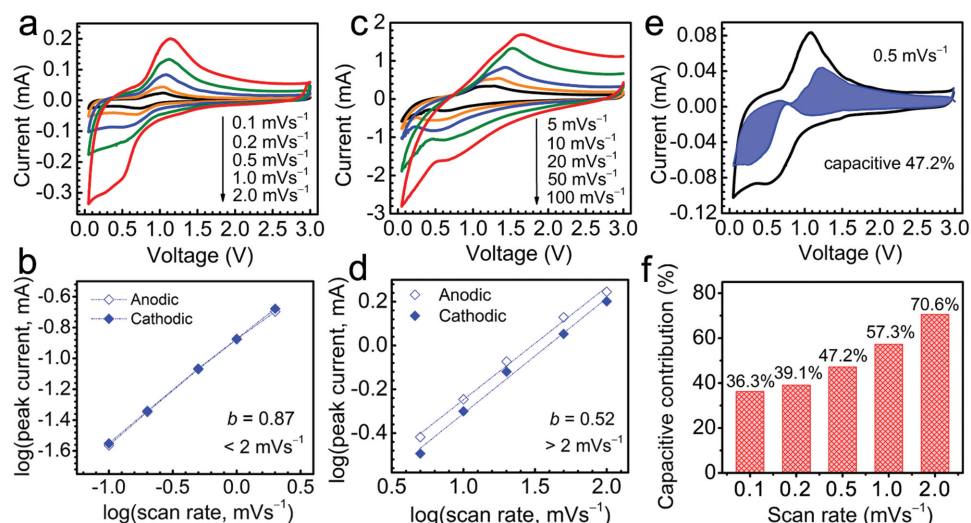


**Figure 6.** Kinetic analysis of the G-PLTO electrode: a, b) CV curves from 0.1 to 2  $\text{mV s}^{-1}$  and the corresponding  $\log(\text{scan rate})$ - $\log(\text{peak current})$  profiles, c, d) CV curves from 5 to 100  $\text{mV s}^{-1}$  and the corresponding  $\log(\text{scan rate})$ - $\log(\text{peak current})$  profiles, e) separations of the capacitive charge from the total charge at 0.5  $\text{mV s}^{-1}$ , and f) comparison of the capacitive charge contributions of various scan rates.

charge at a particular voltage (see more calculation details as described in the Supporting Information).<sup>[19,41]</sup> Figure 6 displays the calculated result of the charge contributions from the two types of mechanisms at 0.5  $\text{mV s}^{-1}$ . The capacitive contribution is determined to be 47.2%, suggesting that the Na storage in the G-PLTO composite aerogel generates from both capacitive (interfacial) and diffusion-controlled (intercalation) processes. We should also note that the capacitive contributions increase from 36.3% to 70.6% as the scan rate increases from 0.1 to 2  $\text{mV s}^{-1}$  (Figure 6f). This indicates that the kinetics for the  $\text{Na}^+$  intercalation process is limited at high rates, whereas the kinetics for the interfacial Na storage process is still sufficient, in good agreement with the above analysis. The overall kinetic analysis results disclose that the intercalation-based and interfacial Na storage behaviors take effect simultaneously

in the G-PLTO composite aerogel, which account for its high capacity, excellent rate capability and long cycle life.

In order to get more insight into the sodiation process of the G-PLTO electrode, we investigated the phase structure and surface states of the electrode materials at different charge-discharge states. The in situ XRD patterns (Figure 7a) show that a new phase,  $\text{Na}_6[\text{LiTi}_5\text{O}_{12}]$ , emerges on discharging and disappears on charging, which can be attributed to the insertion/extraction of  $\text{Na}^+$  into/out of the  $\text{Li}_4\text{Ti}_5\text{O}_{12}$  host ( $\text{Li}_4\text{Ti}_5\text{O}_{12} \leftrightarrow \text{Na}_6[\text{LiTi}_5\text{O}_{12}]$ ). Besides, the sodiation/desodiation processes are accompanied with a redox reaction between  $\text{Ti}^{4+}/\text{Ti}^{3+}$ , as evidenced by the ex situ X-ray photoelectron spectroscopy (XPS) results, demonstrating that trivalent  $\text{Ti}^{3+}$  appears upon  $\text{Na}^+$  insertion and vanishes on charging (Figure 7b). The peaks assigned to the metal-oxide bond in the

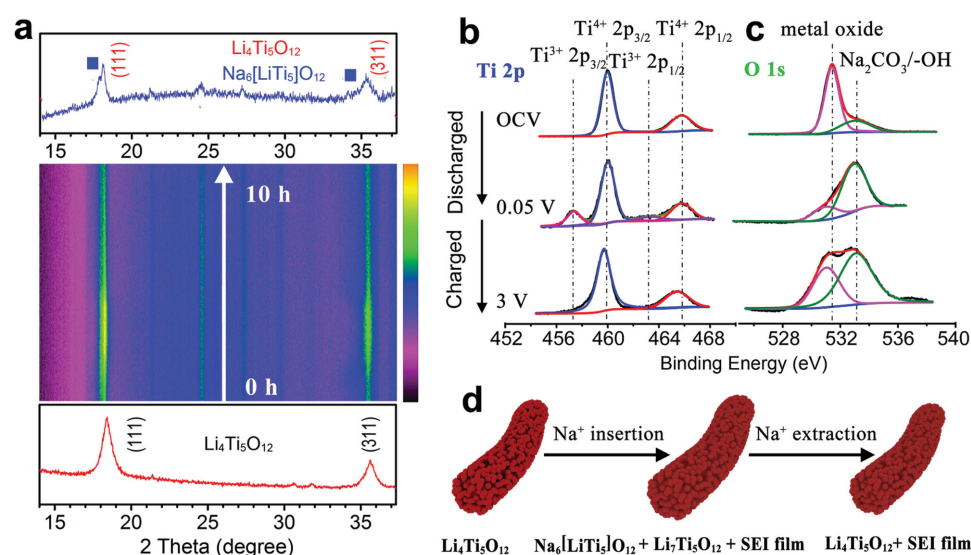


**Figure 7.** a) In situ XRD results, and b, c) ex situ high-resolution XPS spectra of the G-PLTO electrodes at different states of discharge then charge. d) Graphical illustration of the  $\text{Na}^+$  insertion/extraction processes occurring in the G-PLTO electrode.

O 1s high-resolution XPS spectra show similar transformations during discharging and charging, further confirming the redox reaction occurring in the G-PLTO electrode (Figure 7c). Another peak in O 1s related to  $\text{Na}_2\text{CO}_3$  or  $-\text{OH}$  appears on discharging and remains on charging. This may result from the formation of a SEI layer on the surface of the electrode by considering the possibility of reactions between sodium and the carbonate-based electrolyte. Further supports come from the in situ EIS results (Figure S8, Supporting Information). Upon discharging, the semi-circles corresponding to the  $\text{Na}^+$  diffusion in the surface film at high frequency shows a decreasing tendency in diameter, suggesting the decrease in resistance upon  $\text{Na}^+$  insertion into the surface film and the electrode materials. This observed phenomenon may be due to the distinct transport properties of  $\text{Na}^+$  ions in the surface film, similar to the previous report.<sup>[42]</sup> It is worth noting that the EIS spectra keep almost unchanged during the subsequent charging process, indicating of the formation of a stable SEI film on the surface of the electrode. Figure 7d graphically illustrates the new phase formation, redox reaction, SEI layer formation and volume expansion (13%) during the  $\text{Na}^+$  insertion/extraction processes in the G-PLTO electrode.

We further checked the stability of the electrode material after 10 000 discharge–charge cycles. As shown in Figure S9a in the Supporting Information, the graphene-wrapped PLTO microstructure is well maintained even after 10 000 discharge–charge cycles. HR-TEM image shows that the crystal structure of LTO retains well (Figure S9b, Supporting Information), which can be further supported by the selected-area electron diffraction (SAED) (Figure S9c, Supporting Information). While the STEM image and the corresponding linear element distribution results reveal that Na and C elements are rich on the surface (Figure S9d,e, Supporting Information). Considering the fact that the SEI film contains sodium carbonate, it is reasonable to conclude that a SEI layer is formed on the surface of the G-PLTO electrode. This is also consistent with the above analysis. Apparently, both the formation of a stable SEI layer on the surface of the electrode and the high stability of the electrode structure contribute to the outstanding cyclability of the G-PLTO electrode.

### 3. Conclusion

In summary, a novel composite aerogel of porous  $\text{Li}_4\text{Ti}_5\text{O}_{12}$  nanofibers confined in the highly conductive 3D interconnected graphene frameworks has been fabricated via a facile route. As an anode for sodium-ion battery, the composite electrode delivers a high reversible capacitance of  $195 \text{ mA h g}^{-1}$  at 0.2 C and  $120 \text{ mA h g}^{-1}$  at 3 C. More appealingly, an ultra-long cycle life of 12 000 cycles is attained, which is the best cyclability reported in the Ti-based electrodes for SIBs. Further analyses reveal that the unique structure of porous LTO nanofibers wrapped by 3D graphene offers not only short pathways for  $\text{Na}^+$  diffusion and highly conductive networks for electrons transport but also abundant LTO–electrolyte (solid–liquid) and LTO–graphene (solid–solid) interfacial sites for  $\text{Na}^+$  adsorption, giving rise to an additional interfacial Na storage. Moreover, the formation of a stable SEI layer on the

surface of the electrode and the excellent stability of the electrode structure contribute to the outstanding durability. It is believed that the large-capacity and long-life G-PLTO composite aerogel is a promising anode material for high-performance SIBs. Our present findings are helpful for the design and fabrication of next-generation sodium-ion batteries for large-scale energy storage applications.

### 4. Experimental Section

**Materials Synthesis:** GO was synthesized according to a modified Hummer's method,<sup>[43]</sup> and the PLTO nanofibers were prepared as previously reported.<sup>[34]</sup> In a typical procedure, 48 mg of LTO was dispersed into 4 mL of GO solution ( $4 \text{ mg mL}^{-1}$ ) and sonicated for 10 min. Then 20  $\mu\text{L}$  of EDA was added into the above solution. The mixture was ultrasonically treated for another 1 h and then subjected to hydrothermal reaction for 6 h at  $95^\circ\text{C}$ . After cooling down to room temperature, the resultant cylinder hydrogel was taken out and washed with water for several times. The final product was collected by being freeze-dried for 48 h. GA was synthesized in the same procedure as G-PLTO except no PLTO added.

**Materials Characterization:** The structure and morphology of the products were measured by XRD (PANalytical B.V., Holland), SEM (SIRION200), TEM (Tecnai G2 F30, FEI Holland), and XPS (VG MultiLab 2000 system with a monochromatic Al  $K\alpha$  X-ray source, Thermo VG Scientific). TG analysis was carried out in air atmosphere from 40 to  $850^\circ\text{C}$  at a heating rate of  $10^\circ\text{C min}^{-1}$ . Raman spectra were collected on a Renishaw Invia spectrometer with an  $\text{Ar}^+$  laser of 514.5 nm at room temperature.

**Electrochemical Characterization:** All working electrodes were prepared by mixing 80 wt% active material, 10 wt% super P, and 10 wt% polyvinylidene fluoride (PVDF) dissolved in *N*-methyl-2-pyrrolidone to make a slurry, and then coated onto a Cu foil and dried at  $100^\circ\text{C}$  for 24 h before testing (the areal mass loading of the active material in the electrode film is about  $1.5\text{--}2 \text{ mg cm}^{-2}$ ). Sodium metal was used as the counter and reference electrode, glass fiber membrane (GF/D, Whatman) as the separator, and 1 M  $\text{NaClO}_4$  in a mixture of EC and propylene carbonate (PC) (1:1 by volume) as the electrolyte. Galvanostatic charge–discharge measurements were carried out on a Land Battery Measurement System (Land, China) at various C-rates with a cutoff potential window ranging from 0.05–3 V at room temperature. CV at various scan rates from 0.1 to  $100 \text{ mV s}^{-1}$  and electrochemical impedance spectra (EIS) over the frequency ranging from 100 kHz to 0.1 Hz were performed on a PARSTAT 2273 potentiostat.

**In Situ XRD Measurements:** For in situ XRD testing, an electrochemical cell module with a beryllium window directly cast with slurry was used. The XRD patterns of the cell at various discharge–charge states were then collected by a D8 Advance X-ray diffractometer, using  $\text{Cu-K}\alpha$  radiation ( $\lambda = 1.5418 \text{ \AA}$ ).

### Supporting Information

Supporting Information is available from the Wiley Online Library or from the author.

### Acknowledgements

C.C. and H.X. contributed equally to this work. This work was supported by the National Basic Research Program of China (973 Program, 2015CB258400), the Project Funded by China Postdoctoral Science

Foundation (2015M580642), and the PCSIRT (Program for Changjiang Scholars and Innovative Research Team in University, IRT14R18). The authors gratefully acknowledge the Analytical and Testing Center of HUST for XRD, SEM, TEM, TG, and Raman measurements.

Received: February 13, 2016

Revised: March 11, 2016

Published online: May 3, 2016

- [1] P. G. Bruce, B. Scrosati, J. M. Tarascon, *Angew. Chem. Int. Ed.* **2008**, *47*, 2930.
- [2] J. B. Goodenough, *Energy Environ. Sci.* **2014**, *7*, 14.
- [3] B. Dunn, H. Kamath, J. M. Tarascon, *Science* **2011**, *334*, 928.
- [4] C. Chen, Y. Wen, X. Hu, X. Ji, M. Yan, L. Mai, P. Hu, B. Shan, Y. Huang, *Nat. Commun.* **2015**, *6*, 6929.
- [5] C. D. Wessells, S. V. Peddada, R. A. Huggins, Y. Cui, *Nano Lett.* **2011**, *11*, 5421.
- [6] Y. Liang, H. D. Yoo, Y. Li, J. Shuai, H. A. Calderon, F. C. Robles Hernandez, L. C. Grabow, Y. Yao, *Nano Lett.* **2015**, *15*, 2194.
- [7] M. Lin, M. Gong, B. Lu, Y. Wu, D. Wang, M. Guan, M. Angell, C. Chen, J. Yang, B.-J. Hwang, H. Dai, *Nature* **2015**, *520*, 324.
- [8] Z. Jian, W. Luo, X. Ji, *J. Am. Chem. Soc.* **2015**, *137*, 11566.
- [9] L. Li, A. Manthiram, *Adv. Energy Mater.* **2014**, *4*, 1301795.
- [10] Y. Lu, L. Wang, J. Cheng, J. B. Goodenough, *Chem. Commun.* **2012**, *48*, 6544.
- [11] J. Qian, M. Zhou, Y. Cao, X. Ai, H. Yang, *Adv. Energy Mater.* **2012**, *2*, 410.
- [12] R. Berthelot, D. Carlier, C. Delmas, *Nat. Mater.* **2011**, *10*, 74.
- [13] Y. Fang, L. Xiao, X. Ai, Y. Cao, H. Yang, *Adv. Mater.* **2015**, *27*, 5895.
- [14] A. Langrock, Y. Xu, Y. Liu, S. Ehrman, A. Manivannan, C. Wang, *J. Power Sources* **2013**, *223*, 62.
- [15] L. Wu, X. Hu, J. Qian, F. Pei, F. Wu, R. Mao, X. Ai, H. Yang, Y. Cao, *Energy Environ. Sci.* **2014**, *7*, 323.
- [16] Y. Wen, K. He, Y. Zhu, F. Han, Y. Xu, I. Matsuda, Y. Ishii, J. Cumings, C. Wang, *Nat. Commun.* **2014**, *5*, 4033.
- [17] Y. Cao, L. Xiao, M. L. Sushko, W. Wang, B. Schwenzer, J. Xiao, Z. Nie, L. V. Saraf, Z. Yang, J. Liu, *Nano Lett.* **2012**, *12*, 3783.
- [18] W. Luo, J. Scharadt, C. Bommier, B. Wang, J. Razink, J. Simonsen, X. Ji, *J. Mater. Chem. A* **2013**, *1*, 10662.
- [19] D. Xu, C. Chen, J. Xie, B. Zhang, L. Miao, J. Cai, Y. Huang, L. Zhang, *Adv. Energy Mater.* **2016**, *6*, 1501929.
- [20] C. Bommier, W. Luo, W.-Y. Gao, A. Greaney, S. Ma, X. Ji, *Carbon* **2014**, *76*, 165.
- [21] W. Li, M. Zhou, H. Li, K. Wang, S. Cheng, K. Jiang, *Energy Environ. Sci.* **2015**, *8*, 2916.
- [22] H. Xiong, M. D. Slater, M. Balasubramanian, C. S. Johnson, T. Rajh, *J. Phys. Chem. Lett.* **2011**, *2*, 2560.
- [23] K. T. Kim, G. Ali, K. Y. Chung, H. Yashiro, Y.-K. Sun, J. Lu, K. Amine, S.-T. Myung, *Nano Lett.* **2014**, *14*, 416.
- [24] J. Huang, D. Yuan, H. Zhang, Y. Cao, G. Li, H. Yang, X. Gao, *RSC Adv.* **2013**, *3*, 12593.
- [25] H. Pan, X. Lu, X. Yu, Y. Hu, H. Li, X. Yang, L. Chen, *Adv. Energy Mater.* **2013**, *3*, 1186.
- [26] D. Wu, X. Li, B. Xu, N. Twu, L. Liu, G. Ceder, *Energy Environ. Sci.* **2015**, *8*, 195.
- [27] K. Chen, W. Zhang, Y. Liu, H. Zhu, J. Duan, X. Xiang, L. Xue, Y. Huang, *Chem. Commun.* **2015**, *57*, 1608.
- [28] Y. Sun, L. Zhao, H. Pan, X. Lu, L. Gu, Y. Hu, H. Li, M. Armand, Y. Ikuhara, L. Chen, X. Huang, *Nat. Commun.* **2013**, *4*, 1870.
- [29] J. Jamnik, J. Maier, *Phys. Chem. Chem. Phys.* **2003**, *5*, 5215.
- [30] Q. Wu, J. Xu, X. Yang, F. Lu, S. He, J. Yang, H. Fan, M. Wu, *Adv. Energy Mater.* **2015**, *5*, 1401756.
- [31] C. Chen, X. Hu, B. Zhang, L. Miao, Y. Huang, *J. Mater. Chem. A* **2015**, *3*, 22591.
- [32] S. Li, J. Qiu, C. Lai, M. Ling, H. Zhao, S. Zhang, *Nano Energy* **2015**, *12*, 224.
- [33] Z. Chen, V. Augustyn, X. Jia, Q. Xiao, B. Dunn, Y. Lu, *ACS Nano* **2012**, *6*, 4319.
- [34] H. Xu, X. Hu, Y. Sun, W. Luo, C. Chen, Y. Liu, Y. Huang, *Nano Energy* **2014**, *10*, 163.
- [35] S. Komaba, W. Murata, T. Ishikawa, N. Yabuuchi, T. Ozeki, T. Nakayama, A. Ogata, K. Gotoh, K. Fujiwara, *Adv. Funct. Mater.* **2011**, *21*, 3859.
- [36] K.-T. Kim, C.-Y. Yu, C. S. Yoon, S.-J. Kim, Y.-K. Sun, S.-T. Myung, *Nano Energy* **2015**, *12*, 725.
- [37] X. Yu, H. Pan, W. Wan, C. Ma, J. Bai, Q. Meng, S. N. Ehrlich, Y. Hu, X. Yang, *Nano Lett.* **2013**, *13*, 4721.
- [38] C. Wu, P. Kopold, Y. Ding, P. A. van Aken, J. Maier, Y. Yu, *ACS Nano* **2015**, *9*, 6610.
- [39] W. Zhang, Y. Liu, C. Chen, Z. Li, Y. Huang, X. Hu, *Small* **2015**, *11*, 3822.
- [40] J. Wang, J. Polleux, J. Lim, B. Dunn, *J. Phys. Chem. C* **2007**, *111*, 14925.
- [41] V. Augustyn, J. Come, M. A. Lowe, J. W. Kim, P.-L. Taberna, S. H. Tolbert, H. D. Abruña, P. Simon, B. Dunn, *Nat. Mater.* **2013**, *12*, 518.
- [42] R. Demir-Cakan, M. Morcrette, Gangulibabu, A. Gueguen, R. Dedryvere, J.-M. Tarascon, *Energy Environ. Sci.* **2013**, *6*, 176.
- [43] W. S. Hummers, R. E. Offeman, *J. Am. Chem. Soc.* **1958**, *80*, 1339.